

ARTICLE OPEN



Experimental unsupervised learning of non-Hermitian knotted phases with solid-state spins

Yefei Yu^{1,4}, Li-Wei Yu^{1,2,4}, Wengang Zhang^{1,4}, Huili Zhang¹, Xiaolong Ouyang¹, Yanqing Liu¹, Dong-Ling Deng^{1,3}✉ and L.-M. Duan¹✉

Non-Hermiticity has widespread applications in quantum physics. It brings about distinct topological phases without Hermitian counterparts, and gives rise to the fundamental challenge of phase classification. Here, we report an experimental demonstration of unsupervised learning of non-Hermitian topological phases with the nitrogen-vacancy center platform. In particular, we implement the non-Hermitian twister model, which hosts peculiar knotted topological phases, with a solid-state quantum simulator consisting of an electron spin and a nearby ¹³C nuclear spin in a nitrogen-vacancy center in diamond. By tuning the microwave pulses, we efficiently generate a set of experimental data without phase labels. Furthermore, based on the diffusion map method, we cluster this set of experimental raw data into three different knotted phases in an unsupervised fashion without a priori knowledge of the system, which is in sharp contrast to the previously implemented supervised learning phases of matter. Our results showcase the intriguing potential for autonomous classification of exotic unknown topological phases with experimental raw data.

npj Quantum Information (2022)8:116; <https://doi.org/10.1038/s41534-022-00629-w>

INTRODUCTION

Non-Hermiticity naturally emerges in a broad range of scenarios^{1–4}, and has been extensively studied in open quantum systems^{5–8}, photonics systems with loss and gain^{9–13}, and quasiparticles with finite lifetimes^{14–18}, etc. Recently, the interplay between the non-Hermiticity and topological phases has attracted considerable attentions^{17–62}, giving rise to an emergent research frontier of non-Hermitian topological phases of matter in both theory and experiment. Non-Hermitian topological phases bear a number of unique features without Hermitian analogs, including the non-Hermitian skin effect^{38,40,42}, unconventional bulk-boundary correspondence⁴⁰, and funneling of light⁶². To establish the theory of non-Hermitian topological phase classification, previous works have adopted the typical homotopy-based approach akin to the Hermitian tenfold way, and classified the non-Hermitian topological phases into 38 classes⁶⁰. It was later recognized that the non-Hermitian topological phases can be further classified based on the knot or link structures of the complex energy bands, which gave rise to the knotted topological phases^{57–59}. More recently, the braiding of such complex band structure has been implemented in experiment⁵⁶. Yet, hitherto it remains an ongoing challenge to completely classify the non-Hermitian topological phases from both theoretical and experimental aspects^{58–65}.

Machine learning methods provide an alternative and promising approach to classify phases of matter⁶⁶. Within the vein of learning topological phases, considerable strides have been made from both theoretical^{67–82} and experimental^{83–88} aspects, despite the fact that learning topological phases are more intricate than learning the symmetry-breaking ones due to the lack of local order parameters⁸⁹. However, the above learning methods may not be straightforwardly extended to the non-Hermitian scenario owing to the skin effect⁹⁰. This makes the machine learning

non-Hermitian topological phases an intriguing task and a number of theoretical works, including both supervised and unsupervised methods, have been proposed recently^{90–93}. The supervised learning methods require prior labeled samples, hence ruling out the capability of learning unknown phases. While the unsupervised learning can classify different topological phases from unlabeled raw data, without any prior knowledge about the underlying topological mechanism. Consequently, the unsupervised learning methods are more powerful in detecting unknown topological phases. One appealing unsupervised approach is based on the diffusion map^{94–96}, which has been theoretically demonstrated effective in clustering both Hermitian⁷² and non-Hermitian⁹⁰ topological phases. However, to date the capability of machine learning methods in classifying non-Hermitian topological phases has not been demonstrated in experiment.

Here, we report the experimental demonstration of unsupervised learning of non-Hermitian knotted phases with a NV center in diamond. Specifically, we utilize the dilation method^{65,97} to implement the desired non-Hermitian twister Hamiltonian with the NV center platform, where the electron spin constitutes the target system and a nearby ¹³C nuclear spin serves as an ancilla (Fig. 1a). Based on the non-unitary dynamics of the Hamiltonian with different parameters, we prepare an unlabeled data set (including 37 samples) with high fidelity by carrying out 3552 non-unitary evolutions. Then we exploit the diffusion map method to cluster these experimental samples into different knotted topological phases in an unsupervised manner. The learning result matches precisely with the theoretical predictions, which clearly showcases the robustness of the diffusion map method against the experimental imperfections. Besides, with the implemented set of samples, we experimentally realize different knot structures of the twister model, which can serve as the indices for different non-Hermitian topological phases.

¹Center for Quantum Information, IIS, Tsinghua University, 100084 Beijing, P. R. China. ²Theoretical Physics Division, Chern Institute of Mathematics and LPMC, Nankai University, 300071 Tianjin, P. R. China. ³Shanghai Qi Zhi Institute, 200232 Xuhui District, Shanghai, China. ⁴These authors contributed equally: Yefei Yu, Li-Wei Yu, Wengang Zhang. ✉email: dldeng@tsinghua.edu.cn; lmduan@tsinghua.edu.cn

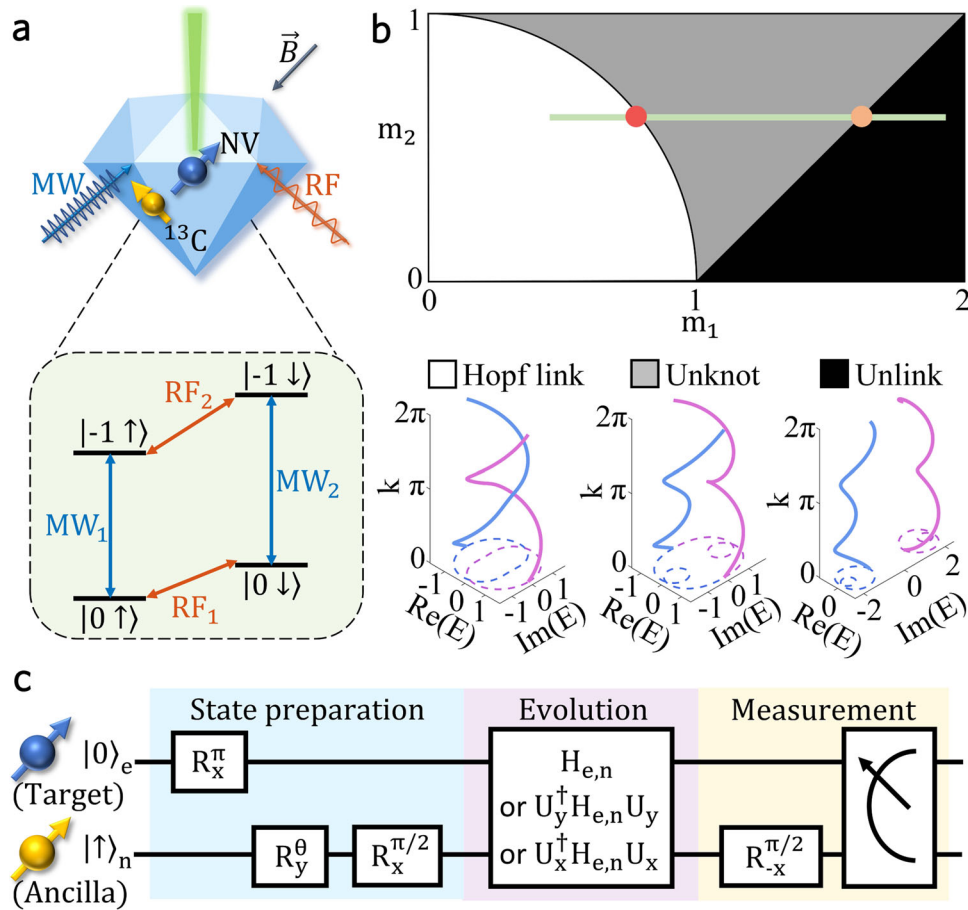


Fig. 1 Simulating the non-Hermitian twister Hamiltonian with knotted topological phases on the NV center platform. **a** Top: schematic illustration of the NV center in diamond. The system is coherently controlled by the microwave (MW) and radio frequency (RF) pulses. The NV electron spin (blue arrow) is coupled to a nearby ^{13}C nuclear spin (yellow arrow). Below: energy level diagram of the electron-nuclear spin system. MW controls the transitions between electron spin states $\{|0\rangle, |-1\rangle\}$, and RF controls the transitions between nuclear spin states $\{|\uparrow\rangle, |\downarrow\rangle\}$. **b** Top: phase diagram of the non-Hermitian twister model. We experimentally simulate the twister Hamiltonian with the parameters $m_{1,2}$ along the green line (crossing the two theoretical phase boundaries). Below: band structures of the twister model in the space spanned by $(\text{Re}(E), \text{Im}(E), k)$, the momentum k is in the first Brillouin zone. Gluing the $k=0$ and $k=2\pi$ planes leads to different knotted band structures, including the Hopf link (white square), the unknot (gray square), and the unlink (dark square). **c** Quantum circuit for simulating the non-Hermitian Hamiltonian in our experiment. Here we take the electron (nuclear) spin as the target (ancillary) qubit.

RESULTS

The model

We consider the one dimensional (1D) non-Hermitian twister model under the periodic boundary condition, with the Hamiltonian taking the form⁵⁷,

$$H(k) = \mathbf{d}(k) \cdot \boldsymbol{\sigma} = im_1\sigma_z + m_2T_1 + T_2, \quad (1)$$

where $\mathbf{d}(k) = (d_x, d_y, d_z)$, $\boldsymbol{\sigma} = (\sigma_x, \sigma_y, \sigma_z)$ are the Pauli matrices, k denotes the 1D momentum in the first Brillouin zone, m_1 and m_2 are tunable parameters (we set $\hbar=1$ for simplicity), and $T_n = \begin{bmatrix} 0 & e^{ink} \\ 1 & 0 \end{bmatrix}$. This model hosts three distinct topological

phases with phase boundaries $m_1^2 + m_2^2 = 1$ and $m_2 = \pm m_1 - 1$. In contrast to the typical homotopy-based approach for phase classification, these phases can be efficiently classified by the knot (link) structures of the complex-energy bands (braid homotopy), where the knot structure is embedded in the space spanned by $(\text{Re}(E), \text{Im}(E), k)$, with E denoting the complex energy. Concretely, the three non-Hermitian topological phases of the twister model are indexed by the Hopf link, the unlink, and the unknot, respectively. The phase transition occurs when the knot structures of the complex bands change across the exceptional points⁵⁷. It is worth noting that all of the three phases host the non-Hermitian

skin effect since the corresponding bands have the point gaps, which indicate that the phase transition points are boundary condition sensitive. A sketch of the phase diagram of the non-Hermitian twister model is shown in Fig. 1b.

Experimental implementation

Experimentally simulating the non-Hermitian Hamiltonian is challenging, since the dynamical evolution of closed systems is usually governed by the Hermitian Hamiltonians. One fruitful approach is to dilate the non-Hermitian Hamiltonian into Hermitian ones in a larger Hilbert space. The dilation method was theoretically proposed to simulate the \mathcal{PT} -symmetric non-Hermitian Hamiltonian⁹⁸. Then it was applied in experiments to study the \mathcal{PT} -symmetry breaking and implement the non-unitary dynamics of photons^{97,99}. More recently, this method is exploited for simulating the dynamics of non-Hermitian Su-Schrieffer-Heeger band model with topological phases⁶⁵.

Here, we utilize the dilation method (see Methods section and Supplementary Note 1) to implement the twister Hamiltonian $H(k)$. With such a dilation method, the simulation of the non-Hermitian $H_e = H(k)$ for the electron spin is mapped to the simulation of a Hermitian Hamiltonian $H_{e,n}$ for the coupled electron and nuclear spins. Figure 1c illustrates the quantum circuit for our experiment.

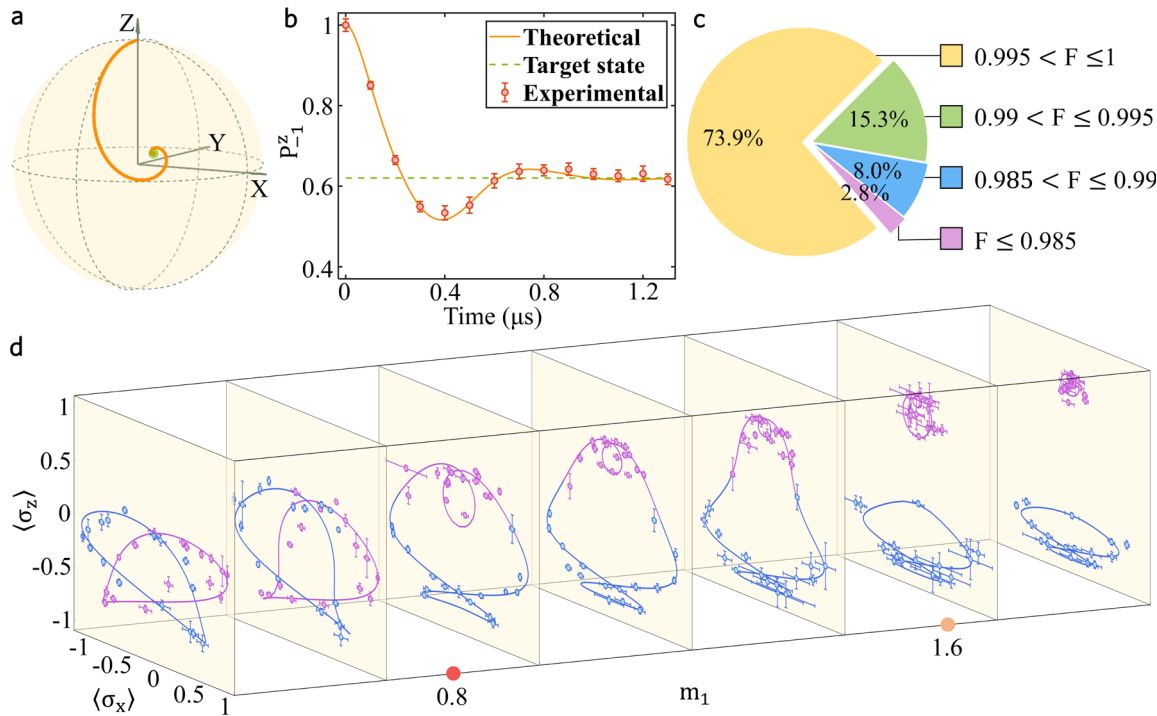


Fig. 2 State preparation through non-unitary dynamics and observation of knot structures for different phases. **a** Decaying trajectory of the electron spin state on the Bloch sphere under non-unitary dynamics. The green dot represents the target state. **b** Non-unitary time evolution of the electron spin population $P_{-1}^z = \text{Tr}(\rho_e | -1 \rangle \langle -1 |)$. The red dots with error bars are the experimental results. Error bars are obtained via Monte Carlo simulation by assuming a Poisson distribution of the photon counts for 10,000 times. The orange solid line shows the theoretical curve predicted by numerical simulation. The green dashed line indicates the ideal population of the target state assuming infinite evolution time. For **a**, **b** the underlying Hamiltonian is $-H(k)$ with the parameters $m_1 = 0.9855$, $m_2 = 0.6$, and $k = 0.125\pi$. **c** Pie chart illustrates the percentage distribution for the fidelity (denoted as F) of the 1184 experimentally prepared eigenstates $\{|R_1\rangle, |R_2\rangle\}$ with varying m_1 and k (see Supplementary Fig. 6). **d** Experimental results for $\langle \sigma_z \rangle$ versus $\langle \sigma_x \rangle$ as k sweeping the first Brillouin zone with different values of m_1 , where the blue and purple parts denote the average values of $\sigma_{x,z}$ with respect to $|R_1\rangle$ and $|R_2\rangle$, respectively. The dots with error bars represent the experimental data, whereas the solid lines denote the theoretical predictions. The red and orange dots denote the phase transition values of m_1 , while fixing $m_2 = 0.6$.

Through optical pumping, we first polarize the state to be $|0\rangle_e |\uparrow\rangle_n$. By rotating along the x - and y -axes, we prepare the initial state $|\Psi(0)\rangle = |-1\rangle_e |- \rangle_n + \eta(0) |-1\rangle_e |+\rangle_n$. We then apply two microwave pulses $MW_{1,2}$ to realize the dilated Hamiltonian $H_{e,n}$. The parameters $m_{1,2}$ and momentum k are tuned by controlling the frequency, amplitude and phase of $MW_{1,2}$. To measure the expectation value of $\sigma_{x,y}$, we apply a unitary transform to the target Hamiltonian⁶⁵: $H_e = U_{y,x}^\dagger H_{e,n} U_{y,x}$. The subsequent nuclear spin $\pi/2$ rotation transforms the dilated state $|\Psi(t)\rangle = |\psi(t)\rangle_e |- \rangle_n + \eta(t) |\psi(t)\rangle_e |+\rangle_n$ into $|\Phi(t)\rangle = |\psi(t)\rangle_e |\uparrow\rangle_n + \eta(t) |\psi(t)\rangle_e |\downarrow\rangle_n$. Finally, we project the nuclear spin into its $|\uparrow\rangle_n, |\downarrow\rangle_n$ subspace and obtain the desired electron spin eigenstate of $H_e = H(k)$ for a given momentum k (see Supplementary Note 1).

Then based on the non-unitary dynamics governed by H_e in the electron spin subsystem, we explore how the state evolves to the desired eigenstate of $H(k)$ by checking the electron spin population on $|-1\rangle_e$ (see Fig. 2a for a schematic demonstration). Figure 2b displays our experimental results of the electron spin population on the state $|-1\rangle_e$, and shows that the experimental results coincide with the theoretical predictions very well, with almost all of the data points being within the error bars. After long time evolution ($\sim 1.2 \mu\text{s}$), the electron spin state decays to the targeted eigenstate of $H(k)$. This shows that the dilation method is effective and efficient in simulating the non-Hermitian twister model.

Unsupervised clustering

Typically, the success of the diffusion map method relies crucially on the data samples. To learn non-Hermitian topological phases in

an unsupervised fashion, one candidate data set is the bulk Hamiltonian unit vectors⁹⁰: $\mathbf{X} = \{\mathbf{x}^{(l)} | \mathbf{x}^{(l)} = \frac{1}{N} \hat{\mathbf{d}}(k_l), |k_l = \frac{2i-N-2}{N}\pi, i \in [1, N]\}\}$ with $\hat{\mathbf{d}} = \frac{\mathbf{d}}{\sqrt{d_x^2 + d_y^2 + d_z^2}}$ and N denotes the

number of unit cells of the system. To fit the experimentally prepared data (the right eigenstates $|R_1\rangle$ and $|R_2\rangle$) into the diffusion map algorithm, we transform the states $|R_{1,2}\rangle$ into the unit Hamiltonian vector:

$$\hat{a}_{x,y,z} = \frac{1}{2} \text{Tr}[\{(|R_1\rangle\langle L_1| - |R_2\rangle\langle L_2|), \sigma_{x,y,z}\}], \quad (2)$$

where the curly brackets denote the anti-commutator, the left and right eigenstates of the Hamiltonian obey the biorthogonal relation $\langle L_\alpha | R_\beta \rangle = \delta_{\alpha\beta}$ with $\alpha, \beta \in \{1, 2\}$, and δ denoting the Kronecker delta function. Therefore, once we obtain the right eigenvectors $|R_1\rangle$ and $|R_2\rangle$ of $H(k_i)$ in the experiment, we can derive the other two eigenstates $|L_1\rangle$ and $|L_2\rangle$. Then by varying the discrete momentum k_i in the first Brillouin zone with step-size $\pi/8$ while fixing m_1 and m_2 , we can prepare one experimental data sample. Consequently, we obtain the experimental data set of 37 samples by varying m_1 , with fixed $m_2 = 0.6$. From Fig. 2c, we see that more than 97.2% of the 1184 prepared states have a fidelity larger than 0.985, which indicates the high quality of our prepared data and the accurate controllability of the system.

One can also probe the topological phase transition of the non-Hermitian twister model by measuring $\langle \sigma_x \rangle$ and $\langle \sigma_z \rangle$ with respect to $|R_1\rangle$ and $|R_2\rangle$, with k sweeping the first Brillouin zone. Figure 2d displays the experimental results of the trajectories of $\langle \sigma_x \rangle$ and $\langle \sigma_z \rangle$ with varying m_1 . The

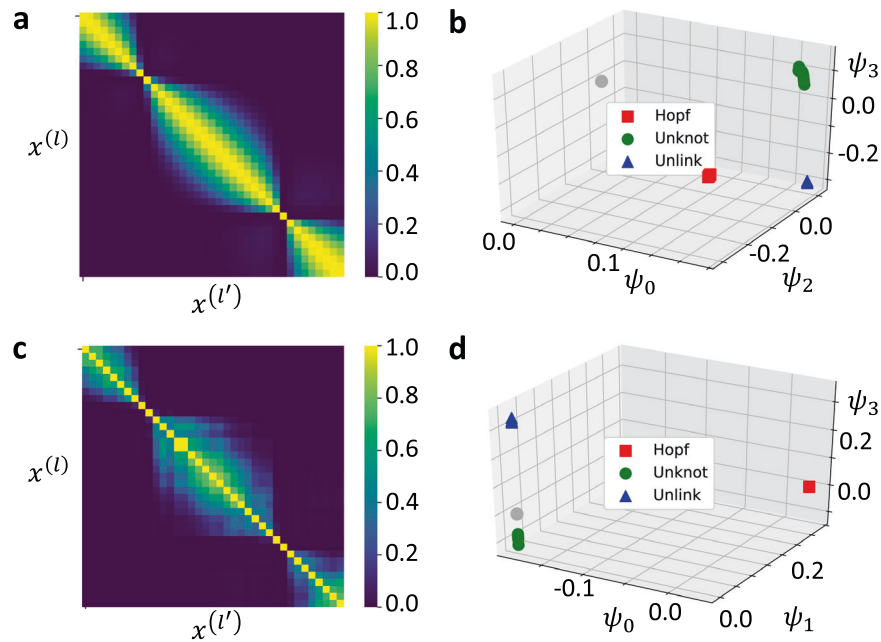


Fig. 3 Unsupervised clustering results for the knotted topological phases with the numerically simulated and experimental data sets. **a** Heatmap for Gaussian kernel value distribution between numerically simulated samples with varying m_1 . Samples belonging to the same yellow block can diffuse to each other with non-zero probability, and hence are clustered together based on the connectivity. The dividing points between the yellow blocks correspond to the phase boundaries. **b** Scatter diagram of the dimension-reduced experimental data samples, obtained from the three right eigenvectors $\psi_{0,2,3}$ of the diffusion matrix with the corresponding eigenvalues $\lambda_{0,2,3} \approx 1$. The numerically simulated data samples are clustered into three knotted topological phases, where the red squares, green circles, and blue triangles denote the Hopf link, unknot, and unlink phases, respectively. **c** Heatmap for Gaussian kernel value distribution between experimental samples. **d** Scatter diagram of the dimension-reduced experimental data samples, obtained from the three right eigenvectors $\psi_{0,1,3}$ of the diffusion matrix with the corresponding eigenvalues $\lambda_{0,1,3} \approx 1$. The experimental data samples are clustered into three topological phases, which agree precisely with the numerical simulation. The gray circles in **b** and **d** denote the 29th sample with $m_1 = 1.6015$, which is very close to the theoretical phase transition point $m_1 = 1.6$. This leads to the pronounced deviation from its presumed category. Parameters are chosen as: number of unit cells $N = 16$, the variance parameter $\epsilon = 0.08$, $m_2 = 0.6$, the varying parameter $m_1^{(l)} = 0.4106 + l * 4/\pi^4$ for each sample $\mathbf{x}^{(l)}$, with $l \in [1, 37]$, the momentum k takes the discrete values $\{\frac{l-9}{8}\pi | i \in [1, 16]\}$.

trajectories of $\langle \sigma_x \rangle$ and $\langle \sigma_z \rangle$ form three types of structures, namely the two overlapping closed loops ($m_1 < 0.8$), one closed loop ($0.8 < m_1 < 1.6$), and two separate closed loops ($m_1 > 1.6$), corresponding respectively to the Hopf link, unknot, and unlink topological phases. This coincides exactly with the theoretical prediction. Based on the experimental data, we can also calculate the global biorthogonal Berry phases that are related to the parity of band permutations⁵⁷ (see Supplementary Table 1).

In Fig. 3, we show the unsupervised learning results for the twister Hamiltonian based on both the numerically simulated and experimental data sets, respectively. Here we generate both the numerical and experimental sets of input samples by orderly varying the parameter m_1 of the twister Hamiltonian, for the convenience of comparing the numerical results and the experimental ones. In a more general context, we also carry out the numerical simulation of unsupervised learning with the input of randomly sampled data, and successfully cluster the samples into three categories (see Supplementary Fig. 8).

Figure 3c shows the kernel value distribution with experimental data samples, where the samples belonging to the same yellow block can diffuse to each other with a sizable probability, and hence can be clustered together based on the connectivity. As a consequence, the experimental data samples are clustered into three categories in the dimension-reduced space, see Fig. 3d. Since the largest eigenvalues $\lambda_i \approx 1$ are almost degenerate, the outputs of the corresponding right eigenvectors in Fig. 3b, d would be up to a non-singular linear transformation. In addition, we can obtain the two phase boundaries from Fig. 3c, which agree precisely with the theoretical prediction, as well as the boundaries of phases indexed by the experimental trajectory results in Fig. 2d.

We note that the 29th sample with $m_1 = 1.6015$ is very close to the phase transition point ($m_1 = 1.6$), which causes a large deviation from its presumed category (see the gray circles in Fig. 3b, d). Besides, by comparing our experimental result with the numerical one in Fig. 3a, b, we obtain that the diffusion map method is sufficiently robust against the experimental noises.

DISCUSSION

We emphasize that the applicability of the diffusion map method in classifying non-Hermitian topological phases can be explained from a physical perspective. On the one hand, it has been rigorously proved that non-Hermitian samples divided by the band crossing points cannot be clustered together via diffusion maps⁹⁰. On the other hand, a more general theory for the non-Hermitian topological phase classification only assumes separable bands³⁰. For the twister model, we have experimentally observed that the band crossing leads to a change of the knot structure (Fig. 2d), which indicates the transition between different topological phases. Hence from the perspective of separable bands, the diffusion map method matches naturally with the mathematical protocol for classifying non-Hermitian topological phases in the momentum space. We remark that when using the diffusion map method for unsupervised learning of unknown phase diagrams, one potential limitation is that the input data should be obtained by densely sampling the configuration space of the target model. Here, the diffusion map method provides a point of principle study. A thorough study of the capabilities of diffusion map method in learning unknown phases of matter remains an

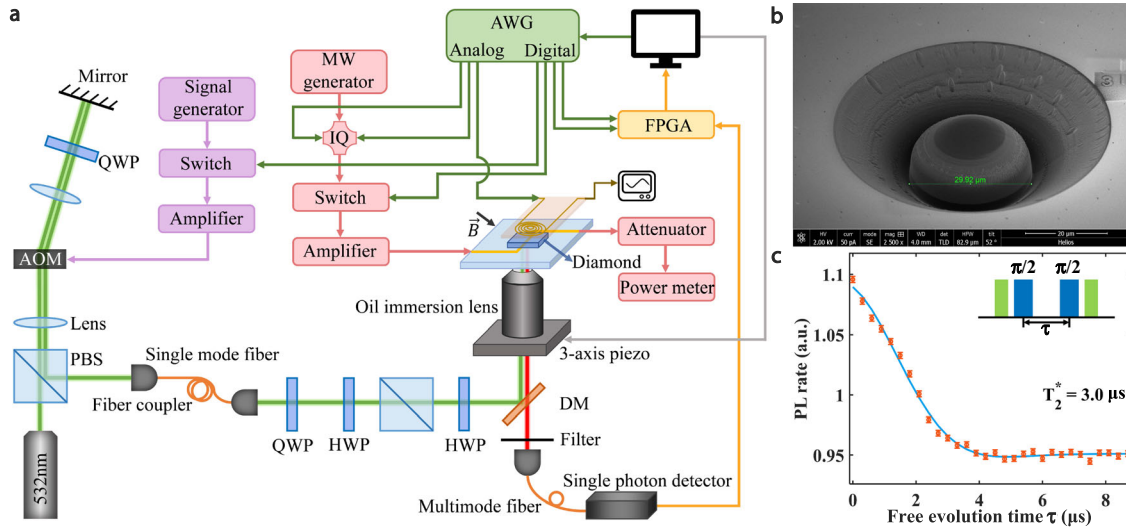


Fig. 4 The diamond sample and experimental setup. **a** Schematic diagram of our experimental setup. **b** Image of a solid immersion lens (SIL) under scanning electron microscope (SEM). The SIL is fabricated by the focused ion beam (FIB). **c** We measure the dephasing time of the electron spin via standard Ramsey interferometry. The experimental data (red circle) is fitted with $f(\tau) = a + b \cos(\delta t + \varphi) \exp(-(\tau/T_2^*)^2)$ (solid blue line), giving $T_2^* = 3.0 \mu\text{s}$.

ongoing task. We leave this interesting and important problem for future studies.

It is worthwhile to note that the non-Hermitian twister model bears unconventional bulk-boundary correspondence, which means that the phase boundaries are sensitive to the boundary conditions. In the future, it would be interesting and important to experimentally demonstrate the unsupervised learning of non-Hermitian topological phases under the open boundary condition. Achieving this requires meticulous and accurate engineering of many spin interactions, which is still a notable challenge with the current NV technologies.

To summarize, we have demonstrated unsupervised learning of non-Hermitian topological phases, based on the non-unitary dynamical evolution of the electron spin with the NV center platform. In particular, we have generated a high-fidelity experimental data set of the non-Hermitian twister model and successfully clustered these experimental samples into different knotted phases in an unsupervised fashion. Our work paves a way to use unsupervised machine learning to identify undiscovered non-Hermitian topological phases with the state-of-the-art experimental platforms.

METHODS

Diffusion map

The diffusion map⁹⁵, as an unsupervised machine learning method, provides a non-linear approach to cluster samples based on the diffusion distance, which is related to the continuous deformation of manifold. Thus, it is particularly suitable for classifying topological objects. To measure the local similarity between the two samples $\mathbf{x}^{(i)}$ and $\mathbf{x}^{(j)}$, we introduce the Gaussian kernel function with the variance ϵ ($0 < \epsilon \ll 1$)

$$\mathcal{K}_{i,j} = \exp\left(-\|\mathbf{x}^{(i)} - \mathbf{x}^{(j)}\|_{\mathbb{L}_1}^2 / (2\epsilon)\right), \quad (3)$$

where $\|\cdot\|_{\mathbb{L}_1}$ denotes the \mathbb{L}_1 -norm distance, i.e., $\|\vec{A}\|_{\mathbb{L}_1} = \sum_i |A_i|$. Then one can define the one-step diffusion probability from the sample $\mathbf{x}^{(i)}$ to $\mathbf{x}^{(j)}$ by $\mathcal{P}_{i,j} = \frac{\mathcal{K}_{i,j}}{\sum_{i'} \mathcal{K}_{i,i'}}$. After evolving $2t$ steps, the diffusion distance between two samples $\mathbf{x}^{(i)}$ and $\mathbf{x}^{(j)}$ is $D_t(j,i) = \sum_k \frac{(\mathcal{P}_{j,k}^{2t} - \mathcal{P}_{i,k}^{2t})^2}{\sum_{k,l} \mathcal{K}_{k,l}} = \sum_k \lambda_k^{2t} [(\psi_k)_j - (\psi_k)_i]^2$, with $\{\psi_k\}$ denoting the right eigenvectors of \mathcal{P} and $\{\lambda_k\}$ being their corresponding

eigenvalues. Then we clearly obtain from D_t that in the long-time limit $t \rightarrow \infty$, only the few eigenvectors with largest $|\lambda| \approx 1$ will dominate, and these few eigenvectors can be utilized for dimension reduction and classifying different non-Hermitian topological phases⁹⁰.

The diamond sample and experimental setup

Our experiments are performed on a $\langle 100 \rangle$ -oriented single crystal diamond (type IIa) produced by Element Six with a natural abundance of carbon isotopes ($[^{13}\text{C}] = 1.1\%$). We utilize a single NV center with a neighboring ^{13}C atom of 13.7 MHz hyperfine strength. A solid immersion lens (SIL) is fabricated on top of the preselected NV center to enhance the collection efficiency (Fig. 4b). The photoluminescence rate of the NV center is about 460 kcps under 80 μW laser excitation.

The diamond sample is mounted on a confocal microscopy system (see Fig. 4a). A 532 nm green laser is used for spin state initialization and readout. The laser beam is then modulated by an acoustic optical modulator (AOM, ISOMET 1250C-848) to generate laser pulses. To avoid continuous polarization caused by the laser leakage, the first-order diffracted beam generated by AOM is reflected by a mirror, forming a double-pass structure to enhance the on-off ratio to $10^5:1$. The green laser is coupled to a single-mode fiber, guided out by a collimator, reflected by a dichroic mirror (DM), and then focused on our sample through an oil-immersion objective lens. The fluorescence photons of the NV center are collected via the same objective lens and pass through the DM followed by a 637 nm long-pass filter. Then the photons are coupled to a multi-mode fiber and detected by a single photon detector module (SPDM). A homemade field-programmable gate array (FPGA) board is applied to count the fluorescence photons.

In order to coherently manipulate the electron spin and nearby nuclear spins, we use an arbitrary waveform generator (AWG, Tektronix 5014C) to generate transistor-transistor logic (TTL) signals and low frequency analog signals. One of the TTL signal controls the on/off of AOM, namely the laser pulses. Another two TTL signals provide gate signals for the FPGA board. For the manipulation of the electron spin, the carrier MW signal generated by a MW source (Keysight N5181B) is combined with two of the analog signals of AWG through an IQ-mixer (Marki Microwave IQ1545LMP). For the manipulation of the nuclear spin, another analog signal is used to generate the RF signal. Both MW and RF signals are further amplified

by amplifiers (Mini Circuits ZHL-30W-252-S+ for MW and Mini Circuits LZY-22+ for RF). The MW signal is then delivered to the diamond sample via a gold coplanar waveguide (CPW). The RF signal is applied through a homemade copper coil.

All the experiments in this work are implemented at room temperature. To polarize the nuclear spins via excited-state level anticrossing (ESLAC)¹⁰⁰, a static magnetic field of $B_z \approx 480$ Gauss is applied along the NV axis by a permanent magnet. To ensure that the coherence time is sufficient for the time evolution process ($\sim 1 \mu\text{s}$) in our experiments, we perform a Ramsey interferometry measurement (Fig. 4c). For the NV center used in this work, the coherence time T_2^* is measured to be $3.0 \mu\text{s}$.

Implementing the non-Hermitian Hamiltonian

Here we implement the twister Hamiltonian $H(k)$ based on the dilation method^{98,101} using the electron-nuclear spin system, with

the electron (nuclear) spin being the target (ancilla) system. Concretely, we consider the quantum state $|\psi(t)\rangle$ in the target system, which evolves under the Hamiltonian H_e with the Schrödinger equation $i\frac{\partial}{\partial t}|\psi(t)\rangle = H_e|\psi(t)\rangle$. We then dilate the state $|\psi(t)\rangle$ into $|\Psi(t)\rangle = |\psi(t)\rangle|-\rangle + \eta(t)|\psi(t)\rangle|+\rangle$ governed by the dilated Hermitian Hamiltonian $H_{e,n}$, where the states $|-\rangle = \frac{1}{\sqrt{2}}(|\uparrow\rangle - i|\downarrow\rangle)$, $|+\rangle = \frac{1}{\sqrt{2}}(|\downarrow\rangle - i|\uparrow\rangle)$ and $\eta(t)$ denotes a proper time-dependent linear operator. With this, the non-unitary time evolution of $|\psi(t)\rangle$ governed by H_e can be obtained by projecting the nuclear spin onto the $|-\rangle$ state. The quantum circuit for implementing H_e in our experiment is shown in Fig. 1c. Here, we omit the detailed parametrization of the dilated Hamiltonian $H_{e,n}$ for brevity, see Supplementary Fig. 1 for details.

In simulating the Hermitian topological phases in Bloch space, the ground states with different momenta can be prepared with the adiabatic passage approach. However, the adiabatic passage

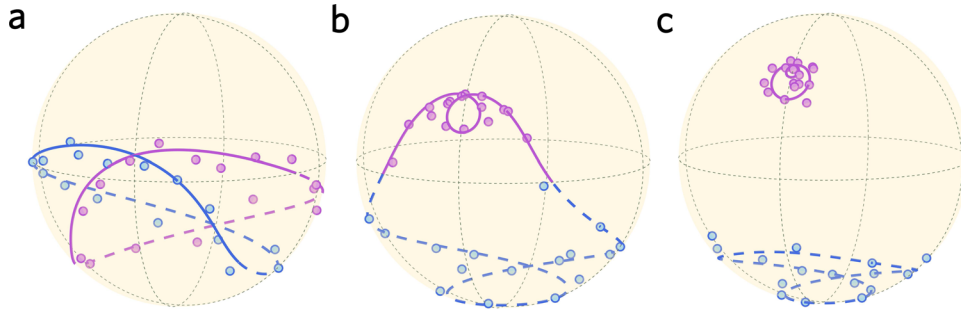


Fig. 5 Trajectories of the eigenvectors on the Bloch sphere. Parameters: **a** $m_1 = 0.5338$, $m_2 = 0.6$ (the Hopf link phase); **b** $m_1 = 1.2730$, $m_2 = 0.6$ (the unknot phase); and **c** $m_1 = 1.8889$, $m_2 = 0.6$ (the unlink phase). The purple and blue curves denote the theoretical trajectories of the two eigenvectors $|R_1(k)\rangle$ and $|R_2(k)\rangle$ as k sweeps from 0 to 2π . The solid and dashed curves are achieved based on the evolution of $H(k)$ and $-H(k)$ respectively. The purple and blue dots represent the experimental results.

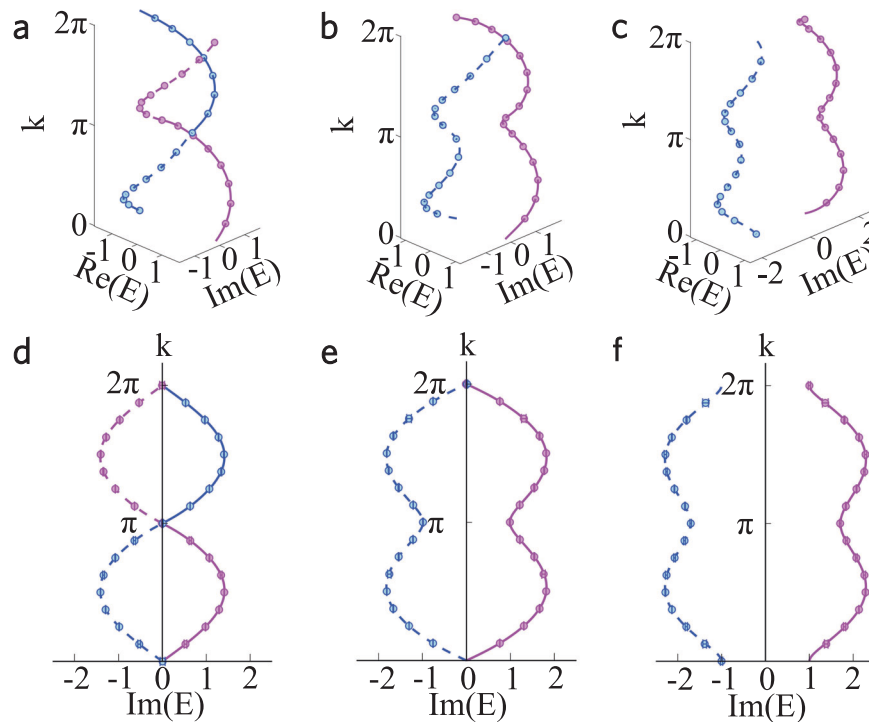


Fig. 6 Non-Hermitian band structures of the twister Hamiltonian. Parameters: **a**, $m_1 = 0.5338$, $m_2 = 0.6$ (the Hopf link phase); **b**, $m_1 = 1.2730$, $m_2 = 0.6$ (the unknot phase); and **c**, $m_1 = 1.8889$, $m_2 = 0.6$ (the unlink phase). **a–c**, Braiding patterns of the complex eigenenergy bands. **d–f**, Projection of the 3D complex eigenenergy bands onto the 2D $(\text{Im}(E), k)$ plane. The purple and blue curves denote the theoretical predictions of the two eigenenergy strings. The solid (dashed) curves denote the non-Hermitian bands with positive (negative) imaginary part of eigenenergy. The corresponding experimental results are represented by the purple and blue dots with error bars.

method for the Hermitian models cannot straightforwardly carry over to the non-Hermitian scenario with complex eigenvalues. To prepare the eigenstates of the twister model, here we utilize the feature of non-unitary evolution governed by the non-Hermitian Hamiltonian. Specifically, suppose the target system is initially at the state $|\psi(0)\rangle = c_1|R_1\rangle + c_2|R_2\rangle$, where $|R_{1,2}\rangle$ are the right eigenvectors of the twister Hamiltonian with eigenvalues $\lambda_{1,2}$. Suppose $\text{Im}(\lambda_1) > \text{Im}(\lambda_2)$, then the system would decay to $|R_1\rangle$ in the long time limit. Hence, one can prepare the eigenstate $|R_1\rangle$ of the twister Hamiltonian based on the long time evolution of the system. Similarly, one can prepare the other eigenstate $|R_2\rangle$ by simply changing H into $-H$. We remark that such progress relies crucially on the imaginary part of the eigenvalues and is suitable for most cases of the parameters (m_1, m_2, k) . For those special cases with real eigenvalues ($k = \pi, 2\pi$ for the Hopf link phase; $k = 2\pi$ for the unknot phase), one can prepare the corresponding eigenstates through the dynamical evolution of $\pm iH$.

Trajectories of eigenstates on the Bloch sphere

Figure 5 shows the three different trajectories of the eigenvectors on the Bloch sphere, with each trajectory corresponding to one topological phase. In Fig. 5a, the two eigenstates $|R_{1,2}(k)\rangle$ with k sweeping the Brillouin zone give rise to two overlapping closed loops, which correspond to the Hopf link phase. In Fig. 5b, the one single closed loop corresponds to the unknot phase. Whereas in Fig. 5c, the two separate closed loops correspond to the unlink phase. The detailed experimental data and the error bars obtained by Monte Carlo simulation are listed in Supplementary Tables 2–7.

Experimental knot band structures

With the experimentally prepared eigenstates $|R_{1,2}(k)\rangle$, we can calculate the corresponding eigenenergies of the non-Hermitian twister Hamiltonian $H(k)$ based on

$$E_n(k) = \langle L_n | H(k) | R_n \rangle, \quad (n = 1, 2).$$

Figure 6 illustrates the braided band structures of the twister Hamiltonian in the first Brillouin zone. Figure 6a–c demonstrates the 3D braiding structures of the complex bands, which are equivalent to the knot (or link) structures by gluing the $k = 0$ and $k = 2\pi$ planes, including the Hopf link, the unknot, and the unlink. As mentioned above, each knot (link) structure indexes one non-Hermitian topological phase. Figure 6d–f illustrates the 2D projection of the 3D braiding complex bands. We see from Fig. 6 that the experimental results (colored dots) match precisely with the theoretical trajectories (solid and dashed lines) of the bands.

DATA AVAILABILITY

All data needed to evaluate the conclusions in the paper are present in the paper and/or the Supplementary Information. Additional data and codes related to this paper are available from the corresponding authors upon reasonable request.

Received: 25 January 2022; Accepted: 8 September 2022;

Published online: 24 September 2022

REFERENCES

- Moiseyev, N. *Non-Hermitian Quantum Mechanics* (Cambridge University Press, 2011).
- Heiss, W. D. The physics of exceptional points. *J. Phys. A: Math. Theor.* **45**, 444016 (2012).
- Konotop, V. V., Yang, J. & Zezyulin, D. A. Nonlinear waves in PT-symmetric systems. *Rev. Mod. Phys.* **88**, 035002 (2016).
- Ashida, Y., Gong, Z. & Ueda, M. Non-Hermitian physics. *Adv. Phys.* **69**, 249 (2020).
- Rotter, I. A non-Hermitian Hamilton operator and the physics of open quantum systems. *J. Phys. A: Math. Theor.* **42**, 153001 (2009).

- Zhen, B. et al. Spawning rings of exceptional points out of Dirac cones. *Nature* **525**, 354–358 (2015).
- Diehl, S., Rico, E., Baranov, M. A. & Zoller, P. Topology by dissipation in atomic quantum wires. *Nat. Phys.* **7**, 971–977 (2011).
- Verstraete, F., Wolf, M. M. & Cirac, J. I. Quantum computation and quantum-state engineering driven by dissipation. *Nat. Phys.* **5**, 633–636 (2009).
- Feng, L., El-Ganainy, R. & Ge, L. Non-Hermitian photonics based on parity–time symmetry. *Nat. Photon.* **11**, 752–762 (2017).
- El-Ganainy, R. et al. Non-hermitian physics and PT symmetry. *Nat. Phys.* **14**, 11–19 (2018).
- Miri, M.-A. & Alu, A. Exceptional points in optics and photonics. *Science* **363**, eaar7709 (2019).
- Özdemir, Ş., Rotter, S., Nori, F. & Yang, L. Parity–time symmetry and exceptional points in photonics. *Nat. Mater.* **18**, 783–798 (2019).
- Ozawa, T. et al. Topological photonics. *Rev. Mod. Phys.* **91**, 015006 (2019).
- Kozii, V. & Fu, L. Non-Hermitian topological theory of finite-lifetime quasiparticles: Prediction of bulk Fermi arc due to exceptional point. Preprint at <https://arxiv.org/abs/1708.05841> (2017).
- Zyuzin, A. A. & Zyuzin, A. Y. Flat band in disorder-driven non-Hermitian Weyl semimetals. *Phys. Rev. B* **97**, 041203(R) (2018).
- Shen, H. & Fu, L. Quantum Oscillation from In-Gap States and a Non-Hermitian Landau Level Problem. *Phys. Rev. Lett.* **121**, 026403 (2018).
- Zhou, H. et al. Observation of bulk fermi arc and polarization half charge from paired exceptional points. *Science* **359**, 1009 (2018).
- Yoshida, T., Peters, R. & Kawakami, N. Non-Hermitian perspective of the band structure in heavy-fermion systems. *Phys. Rev. B* **98**, 035141 (2018).
- Xu, Y., Wang, S.-T. & Duan, L.-M. Weyl exceptional rings in a three-dimensional dissipative cold atomic gas. *Phys. Rev. Lett.* **118**, 045701 (2017).
- Kunst, F. K., Edvardsson, E., Budich, J. C. & Bergholtz, E. J. Biorthogonal bulk-boundary correspondence in non-hermitian systems. *Phys. Rev. Lett.* **121**, 026808 (2018).
- Chen, Y. & Zhai, H. Hall conductance of a non-Hermitian Chern insulator. *Phys. Rev. B* **98**, 245130 (2018).
- Lee, J. Y., Ahn, J., Zhou, H. & Vishwanath, A. Topological correspondence between hermitian and non-hermitian systems: anomalous dynamics. *Phys. Rev. Lett.* **123**, 206404 (2019).
- Lee, T. E. Anomalous edge state in a non-Hermitian lattice. *Phys. Rev. Lett.* **116**, 133903 (2016).
- Carvalho, D., García-Martínez, N. A., Lado, J. L. & Fernández-Rossier, J. Real-space mapping of topological invariants using artificial neural networks. *Phys. Rev. B* **97**, 115453 (2018).
- Lee, C. H. & Thoma, R. Anatomy of skin modes and topology in non-Hermitian systems. *Phys. Rev. B* **99**, 201103(R) (2019).
- Leykam, D., Bliokh, K. Y., Huang, C., Chong, Y. D. & Nori, F. Edge modes, degeneracies, and topological numbers in non-Hermitian systems. *Phys. Rev. Lett.* **118**, 040401 (2017).
- Yin, C., Jiang, H., Li, L., Lü, R. & Chen, S. Geometrical meaning of winding number and its characterization of topological phases in one-dimensional chiral non-Hermitian systems. *Phys. Rev. A* **97**, 052115 (2018).
- Kawabata, K., Higashikawa, S., Gong, Z., Ashida, Y. & Ueda, M. Topological unification of time-reversal and particle-hole symmetries in non-Hermitian physics. *Nat. Commun.* **10**, 297 (2019).
- Gong, Z. et al. Topological phases of non-Hermitian systems. *Phys. Rev. X* **8**, 031079 (2018).
- Shen, H., Zhen, B. & Fu, L. Topological band theory for non-Hermitian Hamiltonians. *Phys. Rev. Lett.* **120**, 146402 (2018).
- Yokomizo, K. & Murakami, S. Non-bloch band theory of non-Hermitian systems. *Phys. Rev. Lett.* **123**, 066404 (2019).
- Ge, Z.-Y. et al. Topological band theory for non-Hermitian systems from the Dirac equation. *Phys. Rev. B* **100**, 054105 (2019).
- Molina, R. A. & González, J. Surface and 3D quantum hall effects from engineering of exceptional points in nodal-line semimetals. *Phys. Rev. Lett.* **120**, 146601 (2018).
- Xue, H., Wang, Q., Zhang, B. & Chong, Y. D. Non-Hermitian dirac cones. *Phys. Rev. Lett.* **124**, 236403 (2020).
- Budich, J. C., Carlström, J., Kunst, F. K. & Bergholtz, E. J. Symmetry-protected nodal phases in non-Hermitian systems. *Phys. Rev. B* **99**, 041406(R) (2019).
- Yoshida, T., Peters, R., Kawakami, N. & Hatsugai, Y. Symmetry-protected exceptional rings in two-dimensional correlated systems with chiral symmetry. *Phys. Rev. B* **99**, 121101(R) (2019).
- Yang, Z. & Hu, J. Non-Hermitian Hopf-link exceptional line semimetals. *Phys. Rev. B* **99**, 081102(R) (2019).
- Okuma, N., Kawabata, K., Shiozaki, K. & Sato, M. Topological origin of non-Hermitian skin effects. *Phys. Rev. Lett.* **124**, 086801 (2020).

39. Li, L., Lee, C. H., Mu, S. & Gong, J. Critical non-Hermitian skin effect. *Nat. Commun.* **11**, 5491 (2020).
40. Yao, S. & Wang, Z. Edge states and topological Invariants of Non-Hermitian Systems. *Phys. Rev. Lett.* **121**, 086803 (2018).
41. Yao, S., Song, F. & Wang, Z. Non-Hermitian chern bands. *Phys. Rev. Lett.* **121**, 136802 (2018).
42. Borgnia, D. S., Kruchkov, A. J. & Slager, R.-J. Non-hermitian boundary modes and topology. *Phys. Rev. Lett.* **124**, 056802 (2020).
43. Song, F., Yao, S. & Wang, Z. Non-Hermitian topological invariants in real space. *Phys. Rev. Lett.* **123**, 246801 (2019).
44. Yang, Z., Chiu, C.-K., Fang, C. & Hu, J. Jones polynomial and knot transitions in Hermitian and non-Hermitian topological semimetals. *Phys. Rev. Lett.* **124**, 186402 (2020).
45. Bessho, T. & Sato, M. Nielsen-ninomiya theorem with bulk topology: duality in floquet and non-hermitian systems. *Phys. Rev. Lett.* **127**, 196404 (2021).
46. Höckendorf, B., Alvermann, A. & Fehske, H. Topological origin of quantized transport in non-Hermitian Floquet chains. *Phys. Rev. Res.* **2**, 023235 (2020).
47. Liu, T. et al. Second-order topological phases in non-Hermitian systems. *Phys. Rev. Lett.* **122**, 076801 (2019).
48. Deng, T.-S. & Yi, W. Non-Bloch topological invariants in a non-Hermitian domain wall system. *Phys. Rev. B* **100**, 035102 (2019).
49. Zeuner, J. M. et al. Observation of a topological transition in the bulk of a non-Hermitian system. *Phys. Rev. Lett.* **115**, 040402 (2015).
50. Poli, C., Bellec, M., Kuhl, U., Mortessagne, F. & Schomerus, H. Selective enhancement of topologically induced interface states in a dielectric resonator chain. *Nat. Commun.* **6**, 6710 (2015).
51. Weimann, S. et al. Topologically protected bound states in photonic parity-time-symmetric crystals. *Nat. Mater.* **16**, 433–438 (2017).
52. Chen, W., Özdemir, Ş. K., Zhao, G., Wiersig, J. & Yang, L. Exceptional points enhance sensing in an optical microcavity. *Nature* **548**, 192–196 (2017).
53. Cerjan, A. et al. Experimental realization of a Weyl exceptional ring. *Nat. Photon.* **13**, 623–628 (2019).
54. Bandres, M. A. et al. Topological insulator laser: experiments. *Science* **359**, eaar4005 (2018).
55. Li, L., Lee, C. H. & Gong, J. Topological switch for non-Hermitian skin effect in cold-atom systems with loss. *Phys. Rev. Lett.* **124**, 250402 (2020).
56. Wang, K., Dutt, A., Wojcik, C. C. & Fan, S. Topological complex-energy braiding of non-Hermitian bands. *Nature* **598**, 59–64 (2021).
57. Hu, H. & Zhao, E. Knots and non-Hermitian bloch bands. *Phys. Rev. Lett.* **126**, 010401 (2021).
58. Li, Z. & Mong, R. S. K. Homotopical characterization of non-hermitian band structures. *Phys. Rev. B* **103**, 155129 (2021).
59. Wojcik, C. C., Sun, X.-Q., Bzdu'sšek, T. & Fan, S. Homotopy characterization of non-Hermitian Hamiltonians. *Phys. Rev. B* **101**, 205417 (2020).
60. Kawabata, K., Shiozaki, K., Ueda, M. & Sato, M. Symmetry and topology in non-Hermitian physics. *Phys. Rev. X* **9**, 041015 (2019).
61. Xiao, L. et al. Non-Hermitian bulk–boundary correspondence in quantum dynamics. *Nat. Phys.* **16**, 761–766 (2020).
62. Weidemann, S. et al. Topological funneling of light. *Science* **368**, 311 (2020).
63. Helbig, T. et al. Generalized bulk–boundary correspondence in non-Hermitian topoelectrical circuits. *Nat. Phys.* **16**, 747–750 (2020).
64. Li, Z. & Mong, R. S. K. Homotopical characterization of non-Hermitian band structures. *Phys. Rev. B* **103**, 155129 (2021).
65. Zhang, W. et al. Observation of non-Hermitian topology with nonunitary dynamics of solid-state spins. *Phys. Rev. Lett.* **127**, 090501 (2021).
66. Carrasquilla, J. & Melko, R. G. Machine learning phases of matter. *Nat. Phys.* **13**, 431–434 (2017).
67. Zhang, Y. & Kim, E.-A. Quantum loop topography for machine learning. *Phys. Rev. Lett.* **118**, 216401 (2017).
68. Zhang, Y., Melko, R. G. & Kim, E.-A. Machine learning Z_2 quantum spin liquids with quasiparticle statistics. *Phys. Rev. B* **96**, 245119 (2017).
69. Yoshioka, N., Akagi, Y. & Katsura, H. Learning disordered topological phases by statistical recovery of symmetry. *Phys. Rev. B* **97**, 205110 (2018).
70. Zhang, P., Shen, H. & Zhai, H. Machine learning topological invariants with neural networks. *Phys. Rev. Lett.* **120**, 066401 (2018).
71. Holanda, N. L. & Griffith, M. A. R. Machine learning topological phases in real space. *Phys. Rev. B* **102**, 054107 (2020).
72. Rodríguez-Nieva, J. F. & Scheurer, M. S. Identifying topological order through unsupervised machine learning. *Nat. Phys.* **15**, 790–795 (2019).
73. Kottmann, K., Huembeli, P., Lewenstein, M. & Acín, A. Unsupervised phase discovery with deep anomaly detection. *Phys. Rev. Lett.* **125**, 170603 (2020).
74. Scheurer, M. S. & Slager, R.-J. Unsupervised machine learning and band topology. *Phys. Rev. Lett.* **124**, 226401 (2020).
75. Che, Y., Gneiting, C., Liu, T. & Nori, F. Topological quantum phase transitions retrieved through unsupervised machine learning. *Phys. Rev. B* **102**, 134213 (2020).
76. Lidiak, A. & Gong, Z. Unsupervised machine learning of quantum phase transitions using diffusion maps. *Phys. Rev. Lett.* **125**, 225701 (2020).
77. Schäfer, F. & Lörch, N. Vector field divergence of predictive model output as indication of phase transitions. *Phys. Rev. E* **99**, 062107 (2019).
78. Balabanov, O. & Granath, M. Unsupervised learning using topological data augmentation. *Phys. Rev. Res.* **2**, 013354 (2020).
79. Alexandrou, C., Athenodorou, A., Chrysostomou, C. & Paul, S. The critical temperature of the 2d-ising model through deep learning autoencoders. *Eur. Phys. J. B* **93**, 226 (2020).
80. Greplova, E. et al. Unsupervised identification of topological phase transitions using predictive models. *New J. Phys.* **22**, 045003 (2020).
81. Arnold, J., Schäfer, F., Žonda, M. & Lode, A. U. J. Interpretable and unsupervised phase classification. *Phys. Rev. Res.* **3**, 033052 (2021).
82. Ma, N. & Gong, J. Unsupervised identification of Floquet topological phase boundaries. *Phys. Rev. Res.* **4**, 013234 (2022).
83. Lian, W. et al. Machine learning topological phases with a solid-state quantum simulator. *Phys. Rev. Lett.* **122**, 210503 (2019).
84. Zhang, Y. et al. Machine learning in electronic-quantum-matter imaging experiments. *Nature* **570**, 484–490 (2019).
85. Rem, B. S. et al. Identifying quantum phase transitions using artificial neural networks on experimental data. *Nat. Phys.* **15**, 917–920 (2019).
86. Bohrdt, A. et al. Classifying snapshots of the doped Hubbard model with machine learning. *Nat. Phys.* **15**, 921–924 (2019).
87. Käming, N. et al. Unsupervised machine learning of topological phase transitions from experimental data. *Mach. Learn.: Sci. Technol.* **2**, 035037 (2021).
88. Lustig, E., Yair, O., Talmon, R. & Segev, M. Identifying topological phase transitions in experiments using manifold learning. *Phys. Rev. Lett.* **125**, 127401 (2020).
89. Beach, M. J. S., Golubeva, A. & Melko, R. G. Machine learning vortices at the Kosterlitz-Thouless transition. *Phys. Rev. B* **97**, 045207 (2018).
90. Yu, L.-W. & Deng, D.-L. Unsupervised learning of non-Hermitian topological phases. *Phys. Rev. Lett.* **126**, 240402 (2021).
91. Long, Y., Ren, J. & Chen, H. Unsupervised manifold clustering of topological phononics. *Phys. Rev. Lett.* **124**, 185501 (2020).
92. Narayan, B. & Narayan, A. Machine learning non-Hermitian topological phases. *Phys. Rev. B* **103**, 035413 (2021).
93. Zhang, L.-F. et al. Machine learning topological invariants of non-Hermitian systems. *Phys. Rev. A* **103**, 012419 (2021).
94. Coifman, R. R. et al. Geometric diffusions as a tool for harmonic analysis and structure definition of data: Multiscale methods. *Proc. Natl. Acad. Sci. USA* **102**, 7432 (2005).
95. Coifman, R. R. et al. Geometric diffusions as a tool for harmonic analysis and structure definition of data: Diffusion maps. *Proc. Natl. Acad. Sci. USA* **102**, 7426 (2005).
96. Coifman, R. R. & Lafon, S. Diffusion maps. *Appl. Comput. Harmon. Anal.* **21**, 5 (2006).
97. Wu, Y. et al. Observation of parity-time symmetry breaking in a single-spin system. *Science* **364**, 878–880 (2019).
98. Kawabata, K., Ashida, Y. & Ueda, M. Information retrieval and criticality in parity-time-symmetric systems. *Phys. Rev. Lett.* **119**, 190401 (2017).
99. Xiao, L. et al. Observation of critical phenomena in parity-time-symmetric quantum dynamics. *Phys. Rev. Lett.* **123**, 230401 (2019).
100. Smeltzer, B., McIntyre, J. & Childress, L. Robust control of individual nuclear spins in diamond. *Phys. Rev. A* **80**, 050302(R) (2009).
101. Günther, U. & Samsonov, B. F. Naimark-dilated \mathcal{PT} -symmetric brachistochrone. *Phys. Rev. Lett.* **101**, 230404 (2008).

ACKNOWLEDGEMENTS

We acknowledge helpful discussions with Z. Wang and S. Zhang. This work was supported by the Frontier Science Center for Quantum Information of the Ministry of Education of China, Tsinghua University Initiative Scientific Research Program, and the Beijing Academy of Quantum Information Sciences, and the National Natural Science Foundation of China (Grants No. 12075128 and No. 11905108). D.-L.D. also acknowledges additional support from the Shanghai Qi Zhi Institute.

AUTHOR CONTRIBUTIONS

Y.Y., L.-W.Y., and W.Z. contributed equally to this work. Y.Y. carried out the experiment under the supervision of D.-L.D. and L.-M.D.; L.-W.Y. did the numerical simulations and analyzed the experimental data together with Y.Y. and W.Z. All authors contributed to the experimental setup, the discussions of the results and the writing of the manuscript.

COMPETING INTERESTS

The authors declare no competing interests.

ADDITIONAL INFORMATION

Supplementary information The online version contains supplementary material available at <https://doi.org/10.1038/s41534-022-00629-w>.

Correspondence and requests for materials should be addressed to Dong-Ling Deng or L.-M. Duan.

Reprints and permission information is available at <http://www.nature.com/reprints>

Publisher's note Springer Nature remains neutral with regard to jurisdictional claims in published maps and institutional affiliations.



Open Access This article is licensed under a Creative Commons Attribution 4.0 International License, which permits use, sharing, adaptation, distribution and reproduction in any medium or format, as long as you give appropriate credit to the original author(s) and the source, provide a link to the Creative Commons license, and indicate if changes were made. The images or other third party material in this article are included in the article's Creative Commons license, unless indicated otherwise in a credit line to the material. If material is not included in the article's Creative Commons license and your intended use is not permitted by statutory regulation or exceeds the permitted use, you will need to obtain permission directly from the copyright holder. To view a copy of this license, visit <http://creativecommons.org/licenses/by/4.0/>.

© The Author(s) 2022